

# MLICv2: Enhanced Multi-Reference Entropy Modeling for Learned Image Compression

Wei Jiang, Yongqi Zhai, Jiayu Yang, Feng Gao, *Member, IEEE*, Ronggang Wang, *Member, IEEE*

**Abstract**—Recent advancements in learned image compression (LIC) have yielded impressive performance gains. Notably, the learned image compression models with multi-reference entropy models (MLIC series) have significantly outperformed existing traditional image codecs such as the Versatile Video Coding (VVC) Intra. In this paper, we present MLICv2 and MLICv2<sup>+</sup>, enhanced versions of the MLIC series, featuring improved transform techniques, entropy modeling, and instance adaptability. For better transform, we introduce a simple token mixing transform block inspired by the meta transformer architecture, addressing the performance degradation at high bit-rates observed in previous MLIC series while maintaining computational efficiency. To enhance entropy modeling, we propose a hyperprior-guided global correlation prediction, enabling the capture of global contexts in the initial slice of the latent representation. We also develop a channel reweighting module to dynamically prioritize important channels within each context. Additionally, advanced positional embedding for context modeling and selective compression with guided optimization are investigated. To boost instance adaptability, we employ stochastic Gumbel annealing to iteratively refine the latent representation according to the rate-distortion optimization of a specific input image. This approach further enhances performance without impacting decoding speed. Experimental results demonstrate that our MLICv2 and MLICv2<sup>+</sup> achieve state-of-the-art performance, reducing Bjøntegaard-Delta rate (BD-rate) by 16.54%, 21.61%, 16.05% and 20.46%, 24.35%, 19.14% respectively, compared to VTM-17.0 Intra on the Kodak, Tecnick, CLIC Pro Val dataset, respectively.

**Index Terms**—Entropy model, learned image compression.

## I. INTRODUCTION

Image compression is a fundamental and active topic in the area of image processing, which aims to compactly represent static visual signals while maintaining acceptable reconstructed quality. Traditional image compression methods, such as VVC Intra [1], are established on the block-based hybrid coding framework, which has been developed for several decades. However, as the performance improvements of traditional image compression methods approach a plateau, learned image compression (LIC) has emerged as a promising alternative, attracting significant attention from both academic and industrial fields. The end-to-end optimization of LICs offers the potential to surpass handcrafted traditional codecs.

Most current LICs [2]–[24] are based on autoencoders [25] with a rate penalty, which consists of an analysis transform,

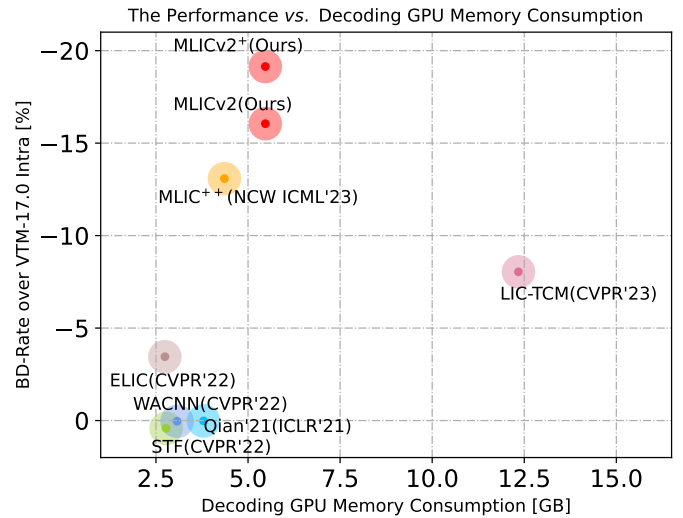


Fig. 1. BD-Rate and decoding GPU memory consumption during inference on CLIC Professional Valid [28] with 2K resolution.

quantization, a synthesis transform and an entropy model. The analysis transform is employed to convert the input image to a latent representation, the latent representation is quantized and converted to pixel space by the synthesis transform. The entropy model is employed to estimate the distribution of the quantized latent representation for entropy coding. Subsequent research has explored various techniques, such as hyperprior [4], deep transform [7], [10], [19], [22] and advanced entropy models [5], [6], [9]–[11], [20], [21] to enhance the performance. Based on advanced techniques, certain methods [10]–[13], [16], [19]–[22], [26], [27] are already comparable or superior to the advanced traditional method VVC Intra [1].

Entropy modeling [4]–[6] is a long-standing challenge in LIC, aimed at capturing more priors for lower conditional entropy of the current element. To enhance the performance, hyperprior [4] and context modules [6], [10], [16], [20], [21] are developed. The hyperprior module transmits additional side information as prior to the decoder. The context modules estimate the correlations between decoded elements and current element. Recently, Jiang *et al.* propose MLIC and MLIC<sup>+</sup> [20] to capture the multi-reference priors for entropy modeling. In MLIC/MLIC<sup>+</sup>, the latent representation is first divided into multiple slices along the channel dimension [6] to capture inter-slice contexts. For the current slice, MLIC/MLIC<sup>+</sup> employs the checkerboard partition [9] to capture intra-slice local context with two-pass decoding. In addition, the attention map of previous slice is employed to predict the global correlations in the current slice.

Manuscript received 29 August 2024.

Wei Jiang, Yongqi Zhai, Ronggang Wang are with Guangdong Provincial Key Laboratory of Ultra High Definition Immersive Media Technology, Peking University Shenzhen Graduate School, 518055, Shenzhen, China.

Yongqi Zhai, Jiayu Yang, Ronggang Wang are with Peng Cheng Laboratory, 518000 Shenzhen, China.

Feng Gao is with School of Arts, Peking University, 100871, Beijing, China. Ronggang Wang is the corresponding author.

The multi-reference entropy modeling significantly enhances the performance. To circumvent the *quadratic* complexity caused by vanilla attention in MLIC/MLIC<sup>+</sup>, vanilla attention is replaced by linear attention in MLIC<sup>++</sup> [21]. MLIC<sup>++</sup> also explores the global correlations among the previous slices, which enhances the performance.

However, although MLIC series achieve superior performance, there are some limitations to be addressed. Regarding transform, MLIC series tend to have performance degradation at high bit-rates, due to the limited capacity of transform modules to retain enough information in latent representation [29]. Regarding entropy modeling, the estimation of global correlations in the current slice relies on the previous slice, which makes it impossible to capture the global correlations in the *first slice*. Meanwhile, MLIC series employ the contexts for entropy modeling directly, ignoring the different importance of each channel. For more accurate entropy modeling, it is better to pay more *attention* to important channels within each context. Regarding instance adaptability, rate-distortion optimization (RDO) for a specific input [30], [31], is widely adopted in traditional image/video compression [31], [32]. In MLIC series, the parameters and latent representation are fixed during testing, which implies the instance adaptability may be insufficient for a specific input. It is promising to enhance the instance adaptability to boost the performance.

To address above issues, we propose MLICv2, which improves MLIC<sup>++</sup> [21] with advanced techniques to enhance the transform, entropy modeling, thereby boosting the performance. The MLICv2 is further enhanced to MLICv2<sup>+</sup> by iterative refinement techniques for improved instance adaptability.

To enhance the transform, we propose the efficient simple token mixing block to replace the residual blocks [7] in the transforms of MLIC<sup>++</sup> [21]. The simple token mixing block is inspired by the meta transformer architecture [33], using a simple  $5 \times 5$  depth-wise convolution for token mixing and a light-weighted gate block [22] for efficient point-wise interactions. The more advanced macro architecture design significantly enhances the performance at high bit-rates. Meanwhile, our proposed simple token mixing block does not rely on complex components, making the complexity lower than the complexity of original residual blocks [7].

To enhance the entropy modeling, we propose an enhanced multi-reference entropy model (MEMv2) to capture multiple correlations. Since the spatial distribution of the hyperprior is similar to the latent representation, therefore, we propose employing the hyperprior to estimate the global correlations in the first slice for lower conditional entropy. To dynamically pay more attention to important channels of the captured contexts, we propose a channel reweighting module, which computes the channel-wise attention map of each context, where a higher attention score indicates higher importance. In addition, we investigate advanced positional embedding and selective compression to enhance entropy modeling further. For positional embedding, the proposed 2D rotary position embedding replaces the additive relative position embedding in the MLIC series. For selective compression, we propose optimizing the selective compression map predictor with the guide of quantized elements, which stabilizes the training.

To enhance the instance adaptability, Stochastic Gumbel Annealing (SGA) [34] is applied to iteratively refine the latent representation and side information for better performance for a specific input. In SGA, latent representation and side information are gradually aware of quantization, stabilizing the training.

Based on the above-mentioned advanced techniques, our MLICv2 and MLICv2<sup>+</sup> significantly outperform MLIC<sup>++</sup> [21], as illustrated in Fig. 1. Our MLICv2 and MLICv2<sup>+</sup> achieve 16.54%, 21.61%, 16.05% and 20.46%, 24.35%, 19.14% bit-rate reductions over VTM-17.0 Intra on Kodak [35], Tecnick [36], CLIC Pro Val [28], respectively. Our contributions are summarized as follows:

- To enhance the transform, we propose the simple token mixing block, which follows the macro architecture of the meta transformer. The residual blocks in transforms are replaced by the simple token mixing blocks to enhance performance at high bit-rates with lower complexity.
- To enhance the entropy modeling, we propose to employ the hyperprior to predict the global correlations in the first slice, reducing the bit-rate. To pay more attention to more beneficial channels of contexts, we propose the channel reweighting module to generate channel-wise attention maps to emphasize specific channels. We also explore the 2D rotary position embedding and guided selective compression for entropy modeling.
- To enhance the instance adaptability, we apply the SGA to refine the latent representation and side information iteratively during encoding, significantly enhancing the performance.
- Experiments demonstrate that our MLICv2 and MLICv2<sup>+</sup> achieve state-of-the-art performances, reducing bd-rate by 16.54%, 21.61%, 16.05% and 20.46%, 24.35%, 19.14% over VTM-17.0 Intra [1] on Kodak [35], Tecnick [36], CLIC Pro Val [28] dataset, respectively.

## II. RELATED WORKS

### A. Learned Image Compression

Autoencoder-based learned image compression [2], [3], [5]–[7], [10], [20]–[22] follows the transform coding paradigm, which consists of an analysis transform  $g_a$  with parameters  $\phi$ , a synthesis transform  $g_s$  with parameters  $\psi$ , a quantization function  $[\cdot]$ , and an entropy model  $p$  with parameters  $\rho$ . Given an input image  $\mathbf{x} \sim p_{\mathbf{x}}$ , the analysis transform  $g_a$  converts it to a compact latent representation  $\mathbf{y}$ ,  $\mathbf{y}$  is quantized and converted back to the RGB domain by synthesis transform  $g_s$ . The process is formulated as:

$$\mathbf{y} = g_a(\mathbf{x}; \phi), \hat{\mathbf{y}} = [\mathbf{y}], \hat{\mathbf{x}} = g_s(\hat{\mathbf{y}}; \psi). \quad (1)$$

The entropy model  $p$  is employed to estimate the distribution for entropy coding. The rate-distortion optimization is achieved through:

$$\mathcal{L} = \mathbb{E}_{\mathbf{x} \sim p_{\mathbf{x}}} \left[ \underbrace{-\log_2 \int p(\hat{\mathbf{y}}; \rho) d\hat{\mathbf{y}}}_{\text{bit-rate}} + \lambda \times \underbrace{\mathcal{D}(\hat{\mathbf{x}}, \mathbf{x})}_{\text{distortion}} \right], \quad (2)$$

where  $\lambda$  balances the trade-off between rate and distortion. During training, quantization is replaced by adding uniform noise (AUN)  $\mathbf{u} \sim \mathcal{U}(-0.5, 0.5)$  [2] or straight-through-estimator (STE) [3] for its indifferenciability. Ballé *et al.* [4] introduce hyper analysis  $h_a$  and hyper synthesis  $h_s$  to improve entropy estimation, utilizing quantized side information  $\hat{\mathbf{z}}$  extracted from the latent representation.

Significant improvements in transform design have been achieved through various architectural innovations. These include the introduction of Generalized Divisive Normalization (GDN) [37], residual non-local attention [18], [38], deep residual networks [7], and more recently, transformer-based architectures [11], [12], [39]. In addition, mixed cnn-transformer architecture [19] is also investigated for both local and non-local interactions. Distribution modeling has evolved from simple univariate Gaussian models [4] to more sophisticated approaches, including mean-scale Gaussian models [5], asymmetric Gaussian distributions [40], Gaussian mixture models [7], and Gaussian-Laplacian-Logistic mixture models [27]. These advancements have significantly improved the accuracy of entropy estimation, leading to better compression performance.

### B. Conditional Entropy Models

Conditional entropy models leverage context  $\hat{\mathbf{C}}$  to reduce bitrate, exploiting the information theory principle that conditional entropy is bounded by unconditional entropy:

$$\mathcal{H}(\hat{\mathbf{y}}|\hat{\mathbf{C}}) \leq \mathcal{H}(\hat{\mathbf{y}}), \quad (3)$$

where  $\mathcal{H}$  denotes Shannon entropy.

Local context modeling has progressed from serial approaches like PixelCNN [5], [41] to more efficient parallel methods such as zigzag scanning [42] and checkerboard partitioning [10]. Above approaches can be referred to intra-slice local contexts by treating the latent representation as a slice. Meanwhile, Minnen *et al.* [6] propose to conduct the channel-wise autoregressive conditional coding, due to the fixed number of channels for faster decoding. The inter-slice local context module is complementary to intra-slice local contexts, such as checkerboard [9]. The combination is further investigated in ELIC [10].

Recently, the correlations among distant elements [16], [20], [21], [43], [44] have been investigated. For instance, Qian *et al.* [43] employ neighbor element to estimate the global correlations between current element and decoded distant elements. Qian *et al.* further refine this approach with bi-directional attention [45]. Guo *et al.* [16] propose to employ the L-2 distance to measure the correlations among elements. Kim *et al.* [44] propose to transmit the global information to the decoder to obtain the global dependencies among elements.

The global context modules are complementary to inter-slice and intra-slice local contexts. To benefit from diverse contexts, Jiang *et al.* [20] propose MLIC and MLIC<sup>+</sup> [20], which divide the global contexts into inter-slice and intra-slice global contexts. Specifically, the latent representation is divided into multiple slices for autoregressive conditional coding. Checkerboard attention is proposed for intra-slice local contexts, and stacked convolutional layers are employed for

inter-slice local contexts. The attention map of the previous slice is employed to predict the global correlations within the current slice. To global attention is employed to capture inter-slice global contexts from previous slices. However, the quadratic of vanilla attention makes it unpractical for high-resolution image coding, which is further addressed by MLIC<sup>++</sup> [21] with linear attention mechanism [46], [46]–[48].

## III. METHOD

### A. Background: MLIC<sup>++</sup>

Our proposed MLICv2 and MLICv2<sup>+</sup> are built on MLIC<sup>++</sup> [21]. MLIC<sup>++</sup> adopts the simplified analysis and synthesis transform of Cheng’20 [7], where the attention modules are removed to reduce complexity. In MLIC<sup>++</sup>, the linear complexity multi-reference entropy model (MEM<sup>++</sup>) is employed to capture the hyperprior, intra-slice and inter-slice dependencies. Specifically, the hyper conditional information  $\hat{\mathbf{H}}$  is first extracted from side information  $\hat{\mathbf{z}}$ . Following Minnen *et al.* [6], the latent representation  $\hat{\mathbf{y}}$  is divided into  $L + 1$  slices  $\{\hat{\mathbf{y}}^0, \hat{\mathbf{y}}^1, \dots, \hat{\mathbf{y}}^L\}$ . For the  $i$ -th slice  $\hat{\mathbf{y}}^i$ , the slice is divided into anchor part  $\hat{\mathbf{y}}_{ac}^i$  and non-anchor part  $\hat{\mathbf{y}}_{na}^i$  via the checkerboard partition [9]. The inter-slice local contexts module  $g_\ell^{inter}$  is employed to capture the inter-slice local context  $\hat{\mathbf{C}}_\ell^{<i}$  from  $\hat{\mathbf{y}}^{<i}$ . To capture inter-slice global context  $\hat{\mathbf{C}}_g^{<i}$  from  $\hat{\mathbf{y}}^{<i}$ , inter-slice global context module adopts the linear attention [47] for better balance between performance and complexity. The intra-slice local context  $\hat{\mathbf{C}}_\ell^i$  is captured from anchor part  $\hat{\mathbf{y}}_{ac}^i$  via the overlapped window-based checkerboard attention  $g_\ell^{intra}$ . Due to the inherent encoding-decoding consistency, obtaining similarities between decoded elements and current unknown elements is challenging. Since feature maps of each slice can be treated as thumbnails, different slices exhibit similar global similarities. Therefore, in MLIC<sup>++</sup>, the attention map of the anchor part of the  $i - 1$ -th slice and the non-anchor part of the  $i - 1$ -th slice are employed to predict the global similarity between the anchor part of the current slice  $\hat{\mathbf{y}}_{ac}^i$  and the non-anchor part of the current slice  $\hat{\mathbf{y}}_{na}^i$ . The intra-slice global context  $\hat{\mathbf{C}}_g^i$  is extracted from  $\hat{\mathbf{y}}_{ac}^i$  via the attention map and intra-slice global context module  $g_g^{intra}$ . The overall process is formulated as:

$$\begin{aligned} \hat{\mathbf{C}}_\ell^{<i} &= g_\ell^{inter}(\hat{\mathbf{y}}^{<i}), \hat{\mathbf{C}}_g^{<i} = g_g^{inter}(\hat{\mathbf{y}}^{<i}), \\ \hat{\mathbf{C}}_\ell^i &= g_\ell^{intra}(\hat{\mathbf{y}}_{ac}^i), \hat{\mathbf{C}}_g^i = g_g^{intra}(\hat{\mathbf{y}}_{ac}^{i-1}, \hat{\mathbf{y}}_{na}^{i-1}, \hat{\mathbf{y}}_{ac}^i). \end{aligned} \quad (4)$$

Estimated means  $\mu_{ac}^i$ ,  $\mu_{na}^i$  and scales  $\sigma_{ac}^i$ ,  $\sigma_{na}^i$  are extracted from the context information using entropy parameters module  $g_{ep}$ . The mixed quantization [6] and latent residual prediction module  $g_{lrp}$  [6] is adopted in MLIC<sup>++</sup> [21]. In mixed quantization, the zero-centered STE [3] is applied for distortion and the AUN [2] is applied for entropy estimation during training. The  $g_{lrp}$  predicts the quantization residual based on the decoded slices and hyperprior. The overall process is:

$$\begin{aligned} \hat{\mathbf{y}}_{ac}^i &= \text{STE}(\mathbf{y}_{ac}^i - \mu_{ac}^i) + \mu_{ac}^i + \mathbf{r}_{ac}^i, \\ \hat{\mathbf{y}}_{na}^i &= \text{STE}(\mathbf{y}_{na}^i - \mu_{na}^i) + \mu_{na}^i + \mathbf{r}_{na}^i, \end{aligned} \quad (5)$$

where

$$\mathbf{r}_{ac}^i = g_{lrp}(\hat{\mathbf{y}}^{<i}, \hat{\mathbf{H}}), \mathbf{r}_{na}^i = g_{lrp}(\hat{\mathbf{y}}^{<i}, \hat{\mathbf{y}}_{ac}^i, \hat{\mathbf{H}}). \quad (6)$$

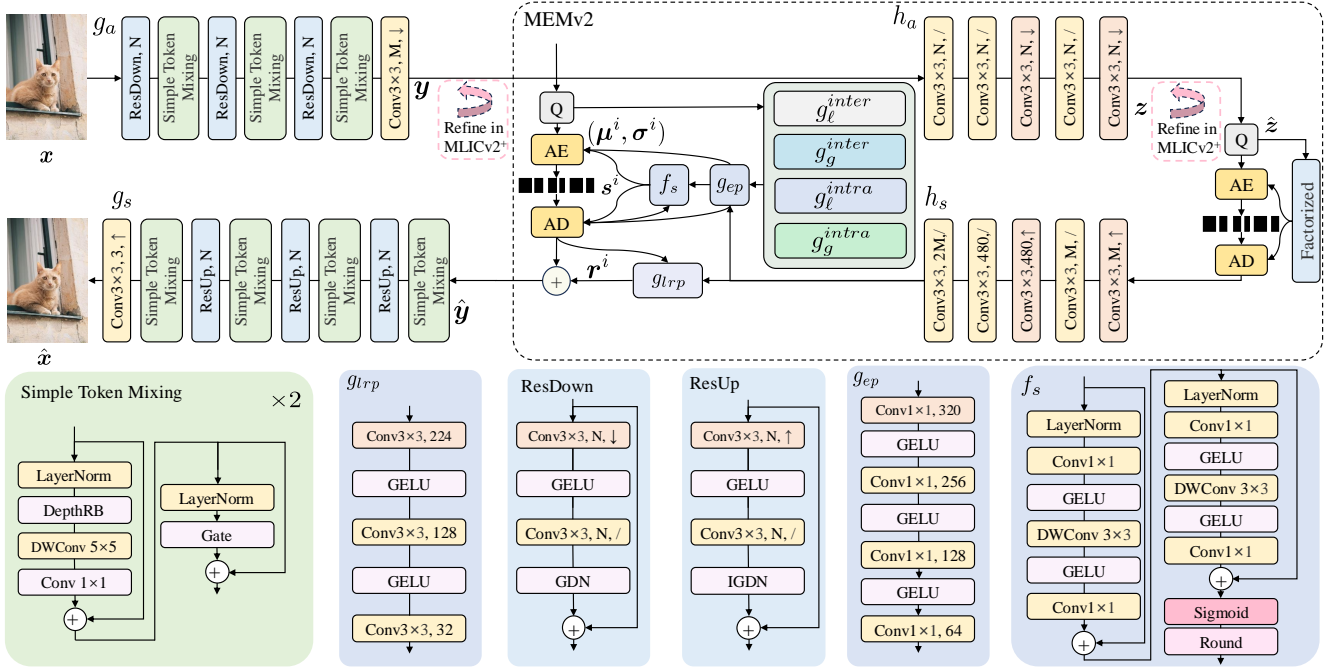


Fig. 2. The overall architecture of MLICv2/MLICv2<sup>+</sup>.  $g_a$  is the analysis transform,  $g_s$  is the synthesis transform,  $h_a$  is the hyper analysis, and  $h_s$  is the hyper synthesis.  $g_{ep}$  is the entropy parameter module.  $f_s$  is the selective compression predictive module.  $g_{lrp}$  is the latent residual prediction module [6]. AE and AD are arithmetic encoding and decoding.  $\uparrow$  denotes upsampling and  $\downarrow$  denotes downsampling.  $\mathbf{x}$  is the input image and  $\hat{\mathbf{x}}$  is the reconstructed image.  $\mathbf{y}$  is the latent representation and  $\hat{\mathbf{y}}$  is the quantized latent representation.  $\hat{\mathbf{y}}^i$  is the  $i$ -th slice of  $\hat{\mathbf{y}}$ .  $\mu^i, \sigma^i$  are the mean and scale of  $\hat{\mathbf{y}}^i$ .  $\mathbf{s}^i$  is the predicted selective coding map.  $\mathbf{r}^i$  is the predicted residual.  $\mathbf{z}$  is the side information.  $M, N$  are the channel numbers, which are 320, 192 in MLICv2/MLICv2<sup>+</sup>. “Refine” is employed in MLICv2<sup>+</sup>.

The overall bit-rate of the  $\hat{\mathbf{y}}$  during training is:

$$\mathcal{R}(\hat{\mathbf{y}}) = \sum_{i=0}^L [\mathcal{R}(\hat{\mathbf{y}}_{ac}^i) + \mathcal{R}(\hat{\mathbf{y}}_{na}^i)], \quad (7)$$

where

$$\begin{aligned} \mathcal{R}(\hat{\mathbf{y}}_{ac}^i) &= \mathbb{E} \left[ -\log_2 \int_{0.5}^{0.5} p(\bar{\mathbf{y}}_{ac}^i | \hat{\mathbf{C}}_\ell^{<i}, \hat{\mathbf{C}}_g^{<i}, \hat{\mathbf{H}}; \rho) du \right], \\ \mathcal{R}(\hat{\mathbf{y}}_{na}^i) &= \mathbb{E} \left[ -\log_2 \int_{0.5}^{0.5} p(\bar{\mathbf{y}}_{na}^i | \hat{\mathbf{C}}_\ell^i, \hat{\mathbf{C}}_g^i, \hat{\mathbf{C}}_\ell^{<i}, \hat{\mathbf{C}}_g^{<i}, \hat{\mathbf{H}}; \rho) du \right], \\ p(\bar{\mathbf{y}}_{ac}^i | \hat{\mathbf{C}}_\ell^{<i}, \hat{\mathbf{C}}_g^{<i}, \hat{\mathbf{H}}; \rho) &\sim \mathcal{N}(\mu_{ac}^i, \sigma_{ac}^i), \\ p(\bar{\mathbf{y}}_{na}^i | \hat{\mathbf{C}}_\ell^i, \hat{\mathbf{C}}_g^i, \hat{\mathbf{C}}_\ell^{<i}, \hat{\mathbf{C}}_g^{<i}, \hat{\mathbf{H}}; \rho) &\sim \mathcal{N}(\mu_{na}^i, \sigma_{na}^i), \end{aligned} \quad (8)$$

where  $\bar{\mathbf{y}}_{ac}^i = \mathbf{y}_{ac}^i + \mathbf{u}$ ,  $\bar{\mathbf{y}}_{na}^i = \mathbf{y}_{na}^i + \mathbf{u}$ ,  $\mathbf{u} \sim \mathcal{U}(-0.5, 0.5)$ ,  $\mathcal{N}$  is the Gaussian distribution.

Although MLIC<sup>++</sup> achieves superior performance, there are some limitations to be addressed. MLIC<sup>++</sup> tends to have performance degradation at high bit-rates. For the first slice  $\hat{\mathbf{y}}^0$  in MLIC<sup>++</sup>, there is no slice as the reference to predict the global correlations in the first slice, indicating room for further enhancement of intra-slice global context capturing. Additionally, context extraction modules of MLIC<sup>++</sup> neglect the importance of different channels, despite channels having varying information content and importance for conditional context modeling. The zero-centered STE in Equation (5) leads to compression of zero elements. Skipping zero elements and replacing them with zeros would not affect distortion while reducing bit-rate and arithmetic coding time. However, predicting

skipped elements requires careful investigation, as STE( $\mathbf{y} - \mu$ ) could be quite large, significantly influencing distortion. Finally, latent representations outputted from learned model weights may not be optimal for specific instances. Optimizing for individual instances may further boost performance.

### B. Overall Architecture

The overall architecture of our proposed MLICv2/MLICv2<sup>+</sup> is presented in Fig. 2. The macro-architecture of MLICv2 is similar to that of MLIC<sup>++</sup>, with the addition of a selective compression module  $f_s$ . In MLICv2, the residual blocks after downsampling and upsampling are replaced with simple token mixing blocks to enhance the performance, particularly at high bit-rates. Enhanced inter-slice and intra-slice context modules incorporating context re-weighting mechanisms and advanced position embedding techniques are employed in the enhanced multi-reference entropy model (MEMv2) to further reduce multi-dimensional redundancy. Additionally, selective compression module  $f_s$  is proposed to predict the zero elements, thereby reducing bit-rate and arithmetic coding time. MLICv2<sup>+</sup> is proposed to further enhance the instance adaptability of MLICv2. In this variant, the latent representation  $\mathbf{y}$  and side information  $\mathbf{z}$  are iteratively refined according to the rate-distortion performance of the input instance.

### C. Efficient Simple Token Mixing Transform

As illustrated in Fig. 6, it seems there are performance degradations for MLIC<sup>++</sup> at high bit-rates due to limited

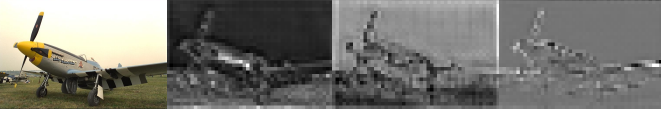


Fig. 3. Visualization of the channels of hyperprior  $\hat{H}$  ( $\lambda = 0.013$ ). The  $\hat{H}$  is extracted from the latent representation of Image Kodim20. The hyperprior  $\hat{H}$  exhibits similar global similarity to the original Kodim20.

capacity of transform modules to retain enough information in latent representation [29]. Recently, transformer layers [49] have been adopted for transform coding [11], [19], [39], [50], demonstrating remarkable performance. A promising solution is to employ the powerful transformer layers. However, the complexity of existing techniques [19] can be up to twice the complexity of original residual blocks in MLIC series, which is prohibitively high. Inspired by the macro design of meta transformer [33], which consists of a token mixing block and a channel-wise interaction layer, we proposed the simple token mixing block, as illustrated in Fig. 2. Specifically, for token mixing, we employ a depth-wise residual block (DepthRB) [22] for nonlinear embedding, a depth-wise convolution for token mixing, and a gate block [22] for efficient channel-wise interactions. LayerNorm (LN) [51] is adopted for stable training. Given the input feature  $\omega$ , the process is formulated as follows:

$$\begin{aligned} \omega &= \omega + \text{Conv1} \times 1(\text{DWConv5} \times 5(\text{DepthRB}(\text{LN}(\omega))))), \\ \omega &= \omega + \text{Gate}(\text{LN}(\omega)), \end{aligned} \quad (9)$$

where  $\omega \in \mathbb{R}^{c \times h \times w}$  is the input feature,  $c, h, w$  are the channel number, height, and width, respectively. Staking two token mixing blocks makes the transform deeper, implying better expressiveness. The token mixing block could be further enhanced by adaptive weights [22], but making convolutions adaptive requires additional layers for weight generation. Therefore, weight generation is not adopted to control the overall parameters.

The proposed simple token-mixing block is employed to replace the residual blocks [7] in the pervious transform. Compared with the previous residual block [7], which consists of two  $3 \times 3$  convolutions, our proposed token mixing block has lower complexity but significantly better performance, especially at high bit-rates. The complexity of the residual block is  $\mathcal{O}(18c^2hw + chw)$  and the complexity of two token mixing blocks is  $\mathcal{O}(16c^2hw + 130chw)$ . When the channel number  $c = 192$ , our token mixing block has 7.38% fewer multiply-accumulate operations (MACs). When  $c = 320$ , our token mixing block has 8.87% fewer MACs.

#### D. Enhanced Multi-Reference Entropy Modeling

The enhanced multi-reference entropy model (MEMv2) is presented in Fig. 4. To capture the global correlations between  $\hat{y}_{ac}^0$  and  $\hat{y}_{na}^0$ , we introduce a hyperprior-based global correlations prediction. For context extraction, channel reweighting is employed to adjust the importance of different context channels. Inspired by the success of the rotary position embedding (RoPE) [52] in large language models [53], [54], we propose a 2D RoPE to apply the original RoPE concept to 2D local

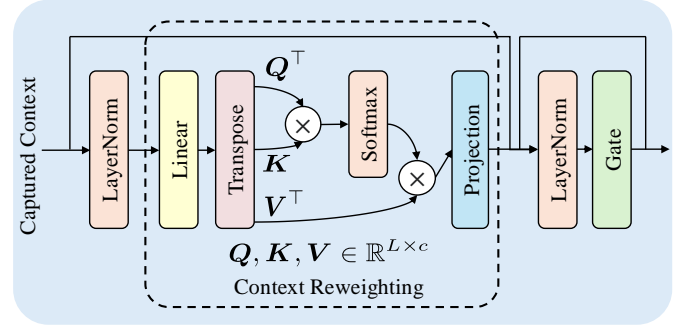


Fig. 4. Proposed context reweighting module.

context mining. Additionally, guided selective compression is investigated to further enhance the model.

1) *Hyperprior Guided Global Context for the First Slice:* For MLIC<sup>++</sup> [21], the global similarity between  $\hat{y}_{ac}^{i-1}$  and  $\hat{y}_{na}^{i-1}$  is employed to predict the global similarity between  $\hat{y}_{ac}^i$  and  $\hat{y}_{na}^i$ , thereby capturing intra-slice global context  $\hat{C}_g^i$  from  $\hat{y}_{ac}^i$  for  $\hat{y}_{na}^i$ . However, for the first slice  $\hat{y}^0$ , no previous slice is available as a reference. In this case, the only conditional information is the hyperprior  $\hat{H}$ . The hyperprior is upsampled from side information  $\hat{z}$ , and the  $\hat{z}$  is extracted from latent representation  $\mathbf{y}$ . The relationship between  $\hat{H}$  and  $\mathbf{y}$  suggests the potential of using  $\hat{H}$  as the reference. To verify the effectiveness of this approach, the feature maps of the  $\hat{H}$  are illustrated in Fig. 3. It is evident that the hyperprior exhibits similar global similarity to the original image. Consequently, the similarity between the anchor part of the hyperprior  $\hat{H}_{ac}$  and the non-anchor part of the hyperprior  $\hat{H}_{na}$  are employed to predict the global similarity between  $\hat{y}_{ac}^0$  and  $\hat{y}_{na}^0$ . Following MLIC<sup>++</sup>, the linear attention [47] is employed. The Gate block is employed for more efficient point-wise interactions [22]. The process is formulated as:

$$\begin{aligned} \hat{C}_g^0 &= \text{Softmax}_2(\hat{H}_{na,q}) \left( \text{Softmax}_1(\hat{H}_{ac,k})^\top \hat{y}_{g,v}^0 \right), \\ \hat{C}_g^0 &= \text{Gate}(\hat{C}_g^0) + \hat{C}_g^0, \end{aligned} \quad (10)$$

where  $\hat{H}_{na,q} = \text{Linear}(\hat{H}_{na})$ ,  $\hat{H}_{ac,k} = \text{Linear}(\hat{H}_{ac})$ ,  $\hat{y}_{g,v}^0 = \text{Linear}(\hat{y}_{ac}^0)$ , Linear is the linear layer for embedding, Gate is the gate block.

2) *Context Reweighting:* In MLIC<sup>++</sup> [21], the contexts are extracted by spatial attention mechanism. Given the query  $Q \in \mathbb{R}^{L \times c}$ , key  $K \in \mathbb{R}^{L \times c}$  and the value  $V \in \mathbb{R}^{L \times c}$ , where  $L = hw$  is the sequence length,  $h$  is the height,  $w$  is the width, and  $c$  is the channel number, in most spatial attention [47], [55], the attention map is computed by  $\text{Sim}(QK^\top) \in \mathbb{R}^{L \times L}$ , where Sim is the predefined function, such as Softmax [55] or two independent Softmax operations [47], meaning the importance of each spatial tokens ( $\in \mathbb{R}^{1 \times c}$ ) and indicating the information is gathered and weighted from spatial tokens. However, we emphasize the characteristics of different channels, recognizing that for a specific input, the importance of different channels may vary. To address this issue, we propose re-weighting *each* captured context along the channel dimension. Specifically, the context is transformed to query  $Q$ , key  $K$ , and value  $V$ , and the query and values are transposed to compute the channel-

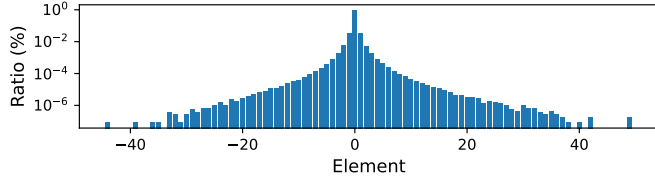


Fig. 5. Ratios of different elements in  $[\mathbf{\Lambda}] = [\mathbf{y} - \boldsymbol{\mu}]$  when the model is optimized for MSE and the  $\lambda = 0.013$ . There are many zero elements in  $[\mathbf{\Lambda}]$ .

wise attention map inspired by [56]. The process is formulated as:

$$\mathbf{A} = \text{Softmax}(\mathbf{Q}^\top \mathbf{K}) \mathbf{V}^\top. \quad (11)$$

The resolution of the attention map  $\text{Softmax}(\mathbf{Q}^\top \mathbf{K})$  is  $c \times c$ , indicating the importance of each channel ( $\in \mathbb{R}^{L \times 1}$ ). The complexity of Equation (11) is  $\mathcal{O}(c^2 hw)$ .  $\mathbf{A}$  is then fed into a Gate block [22] for efficient point-wise interactions. The architecture is depicted in Fig. 4.

3) *2D Rotary Position Embedding*: In MLIC++ [21], relative position embedding from Swin-Transformer [49] is applied to the attention map directly as an additional bias. However, the direct addition may limit interaction with attention weights. Recently, rotary position embedding (RoPE), a multiplication-based relative position embedding, has been widely adopted in language models [53], [54], promoting us to investigate its potential for superior context modeling in image compression. Given the  $m$ -th query  $\mathbf{q}_m \in \mathbb{R}^{1 \times c}$  and  $n$ -th key  $\mathbf{k}_n \in \mathbb{R}^{1 \times c}$ , where  $c$  is the channel number. The original RoPE for language modeling is computed as follows when  $c = 2$ :

$$\begin{aligned} \mathbf{q}'_m &= \mathbf{q}_m \begin{bmatrix} \cos m\theta & -\sin m\theta \\ \sin m\theta & \cos m\theta \end{bmatrix}, \mathbf{k}'_n = \mathbf{k}_n \begin{bmatrix} \cos n\theta & -\sin n\theta \\ \sin n\theta & \cos n\theta \end{bmatrix}, \\ \mathbf{q}'_m (\mathbf{k}'_n)^\top &= \mathbf{q}_m \begin{bmatrix} \cos m\theta & -\sin m\theta \\ \sin m\theta & \cos m\theta \end{bmatrix} \begin{bmatrix} \cos n\theta & -\sin n\theta \\ \sin n\theta & \cos n\theta \end{bmatrix}^\top \mathbf{k}_n^\top, \\ &= \mathbf{q}_m \begin{bmatrix} \cos(m\theta - n\theta) & -\sin(m\theta - n\theta) \\ \sin(m\theta - n\theta) & \cos(m\theta - n\theta) \end{bmatrix} \mathbf{k}_n^\top, \end{aligned} \quad (12)$$

where  $\theta$  is a predefined angle. The  $(m - n)\theta$  indicates the relative position between  $\mathbf{q}_m$  and  $\mathbf{k}_n$ . For  $c > 2$ , the queries and keys are divided into  $\frac{c}{2}$  groups, each following Equation (12).

However, the original RoPE cannot be directly applied to image compression due to *horizontal*, *vertical*, and *diagonal* direction relationships. Inspired by existing 2D position embedding techniques [49], we propose rotating queries and keys twice with different  $\theta_x$  and  $\theta_y$  for horizontal and vertical directions. For 2D positions  $(m_x, m_y)$  and  $(n_x, n_y)$ ,  $(m_x - n_x, m_y - n_y)$  expresses their relationship. Specifically, given query  $\mathbf{q}_{m_x, m_y} \in \mathbb{R}^{1 \times c}$ , key  $\mathbf{k}_{n_x, n_y} \in \mathbb{R}^{1 \times c}$ , when  $c = 2$ , the rotate matrix for query is:

$$\begin{aligned} &\underbrace{\begin{bmatrix} \cos m_x \theta_x & -\sin m_x \theta_x \\ \sin m_x \theta_x & \cos m_x \theta_x \end{bmatrix}}_{\text{horizontal}} \underbrace{\begin{bmatrix} \cos m_y \theta_y & -\sin m_y \theta_y \\ \sin m_y \theta_y & \cos m_y \theta_y \end{bmatrix}}_{\text{vertical}} \\ &= \begin{bmatrix} \cos(m_x \theta_x + m_y \theta_y) & -\sin(m_x \theta_x + m_y \theta_y) \\ \sin(m_x \theta_x + m_y \theta_y) & \cos(m_x \theta_x + m_y \theta_y) \end{bmatrix}. \end{aligned} \quad (13)$$

The rotate matrix for key is:

$$\begin{bmatrix} \cos(n_x \theta_x + n_y \theta_y) & -\sin(n_x \theta_x + n_y \theta_y) \\ \sin(n_x \theta_x + n_y \theta_y) & \cos(n_x \theta_x + n_y \theta_y) \end{bmatrix}. \quad (14)$$

Therefore, the attention score is computed by:

$$\begin{aligned} \mathbf{q}'_{m_x, m_y} &= \mathbf{q}_{m_x, m_y} \begin{bmatrix} \cos(m_x \theta_x + m_y \theta_y) & -\sin(m_x \theta_x + m_y \theta_y) \\ \sin(m_x \theta_x + m_y \theta_y) & \cos(m_x \theta_x + m_y \theta_y) \end{bmatrix}, \\ \mathbf{k}'_{n_x, n_y} &= \mathbf{k}_{n_x, n_y} \begin{bmatrix} \cos(n_x \theta_x + n_y \theta_y) & -\sin(n_x \theta_x + n_y \theta_y) \\ \sin(n_x \theta_x + n_y \theta_y) & \cos(n_x \theta_x + n_y \theta_y) \end{bmatrix}, \\ \mathbf{q}'_{m_x, m_y} (\mathbf{k}'_{n_x, n_y})^\top &= \\ \mathbf{q}_m \begin{bmatrix} \cos \theta_{(m_x - n_x, m_y - n_y)} & -\sin \theta_{(m_x - n_x, m_y - n_y)} \\ \sin \theta_{(m_x - n_x, m_y - n_y)} & \cos \theta_{(m_x - n_x, m_y - n_y)} \end{bmatrix} \mathbf{k}_n^\top, \end{aligned} \quad (15)$$

where  $\theta_{(m_x - n_x, m_y - n_y)} = (m_x - n_x)\theta_x + (m_y - n_y)\theta_y$ , indicating the relative position between  $\mathbf{q}_{m_x, m_y}$  and  $\mathbf{k}_{n_x, n_y}$ . For  $c > 2$ , the queries and keys are divided into  $\frac{c}{2}$  groups, each following Equation (15).

4) *Guided Selective Compression*: According to the zero-centered quantization in Equation (5),  $[\mathbf{\Lambda}] = [\mathbf{y} - \boldsymbol{\mu}]$  may contain many zero elements. The ratios of different elements are illustrated in Fig. 5, demonstrating a significant presence of zero elements in  $[\mathbf{\Lambda}]$ . Recent studies have explored selective compression [57], [58], employing neural networks to predict selective compression maps  $s$ , where 1 means ‘‘do not skip’’ and 0 means ‘‘skip this element’’. Additionally, scale  $\sigma$ -based prediction has been employed in recent methods [59]. Although existing techniques [57]–[59] achieve remarkable performance improvements, they are primarily applied to hyperprior [4] or autoregressive context [5] modules. When applying existing techniques [57]–[59] to our MLICv2 and MLICv2+, the training phase becomes highly unstable, with the overall loss value becoming ‘‘nan’’ after several steps, regardless of whether the parameters of MLICv2 and MLICv2+ are frozen or not. This instability could be attributed to the more complex entropy models in our MLICv2 and MLICv2+, where skipping non-zero elements of the current slice significantly influences the entropy modeling of subsequent slices.

To address above issues, the guided selective compression module  $f_s$  is proposed for post-training. This module is employed on the converged MLICv2, with the weights of MLICv2 frozen for stable training. The architecture of the guided selective compression  $f_s$  module is presented in Fig. 2. Specifically, in  $f_s$ , the scale-based selective prediction is employed as the initial predicted selective compression map. For  $j$ -th element  $s_{\sigma, j}$  in  $s_\sigma$ , the scale-based selective compression value is:

$$s_{\sigma, j} = \begin{cases} 0, & \sigma_j < \xi, \\ 1, & \sigma_j \geq \xi, \end{cases} \quad (16)$$

where  $\xi$  is a predefined threshold, set to 0.3. For  $\mathbf{y}_{ac}^i$ , the decoded elements of previous slices serve as priors. For  $\mathbf{y}_{na}^i$ , the decoded elements of previous slices and  $\mathbf{y}_{ac}^i$  serve as priors.

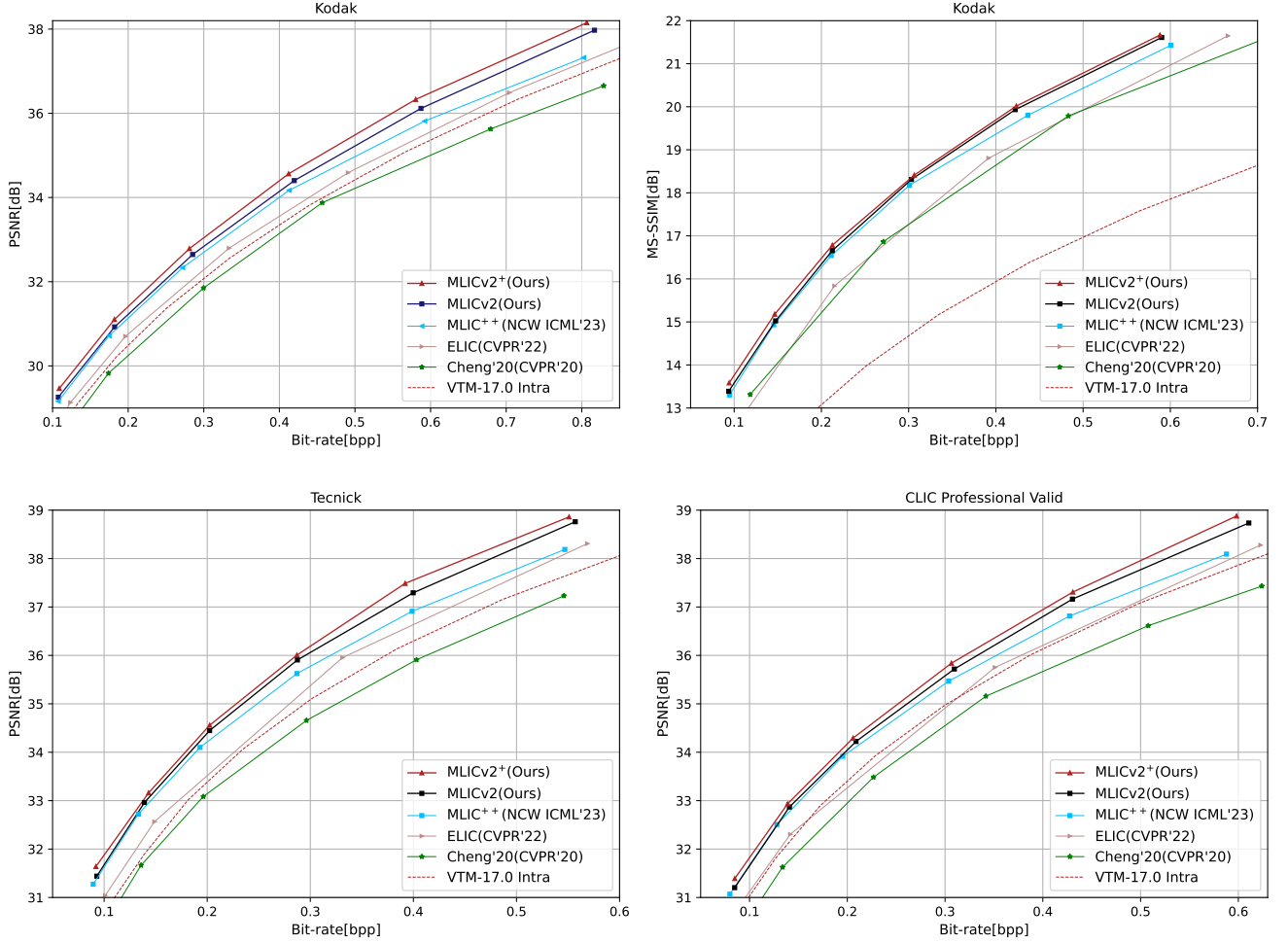


Fig. 6. PSNR-Bit-rate curve and MS-SSIM-Bit-rate curve. MS-SSIM is converted to dB for better visual clarity. Please zoom in for better view.

The hyperprior  $\hat{H}$  also serves as a prior. The predicted selective map is formulated as:

$$\begin{aligned}
 \varepsilon_{ac}^i &= f_s \left( \mathbf{s}_{\sigma,ac}^i, [\Lambda^{<i}] \odot \mathbf{s}^{<i}, \hat{H} \right), \\
 \mathbf{s}_{ac}^i &= \text{STE} \left( \text{Sigmoid} \left( \varepsilon_{ac}^i \right) \right), \\
 \varepsilon_{na}^i &= f_s \left( \mathbf{s}_{\sigma,na}^i, [\Lambda^{<i}] \odot \mathbf{s}^{<i}, [\Lambda_{ac}^i] \odot \mathbf{s}_{ac}^i, \hat{H} \right), \\
 \mathbf{s}_{na}^i &= \text{STE} \left( \text{Sigmoid} \left( \varepsilon_{na}^i \right) \right).
 \end{aligned} \tag{17}$$

During training,  $[\Lambda]$  is known, therefore cross-entropy loss is employed to optimize  $f_s$ , treating selective prediction as a *binary classification* task. Additionally, elements with larger values have a higher impact on distortion, so the cross-entropy loss is weighted by  $[\Lambda] + 1$ . The overall loss is:

$$\begin{aligned}
 \mathcal{L}_s &= \sum_{i=0}^L \left( ([\Lambda_{ac}^i] + 1) \odot \mathcal{L}_{ce,ac}^i + ([\Lambda_{na}^i] + 1) \odot \mathcal{L}_{ce,na}^i \right), \\
 \mathcal{L}_{ce,ac}^i &= - \frac{[\Lambda_{ac}^i] \odot \log \varepsilon_{ac}^i + (1 - [\Lambda_{ac}^i]) \odot \log(1 - \varepsilon_{ac}^i)}{2}, \\
 \mathcal{L}_{ce,na}^i &= - \frac{[\Lambda_{na}^i] \odot \log \varepsilon_{na}^i + (1 - [\Lambda_{na}^i]) \odot \log(1 - \varepsilon_{na}^i)}{2}.
 \end{aligned} \tag{18}$$

### E. Iterative Latent Refinement

To enhance the instance adaptability, the encoder must find the optimal or near-optimal quantized latent representation  $\hat{\mathbf{y}}$  and side information  $\hat{\mathbf{z}}$  for the decoder. Intuitively, the  $\hat{\mathbf{y}}$  and  $\hat{\mathbf{z}}$  can be updated by optimizing the encoder. However, the optimization of the encoder requires to save the model weights, gradients, mid-features, momentums of Adam optimizer [61], leading to significant GPU memory consumption particularly for high-resolution images. Therefore, the Stochastic Gumbel Annealing (SGA) [34] is adopted to refine the  $\mathbf{y}$  and  $\mathbf{z}$ . In SGA [34], the output of the  $g_a$  and  $h_a$  are employed as the initial  $\mathbf{y}$  and  $\mathbf{z}$ . For the anchor part of the  $i$ -th slice  $\mathbf{y}_{ac}^i$ , during the refinement,  $\Lambda_{ac}^i = \mathbf{y}_{ac}^i - \mu_{ac}^i$  is either rounded up ( $\lceil \cdot \rceil$ ) or down ( $\lfloor \cdot \rfloor$ ). Let  $\mathbf{o}_{ac}^i \in \{(0,1), (1,0)\}$  denote the true rounding direction, where  $(0,1)$  means rounding down and  $(1,0)$  means rounding up. The stochastic rounding direction  $(\mathbf{o}_{ac}^i)'$  is sampled from a relaxed one-hot categorical

TABLE I  
BD-RATE (%) COMPARISON FOR PSNR (DB) AND MS-SSIM. THE ANCHOR IS VTM-17.0 INTRA. “—” MEANS THE RESULT IS NOT AVAILABLE.

Methods	Venue	BD-Rate (%) w.r.t. VTM 17.0 Intra			
		Kodak [35]		Tecnick [36]	CLIC Pro Valid [28]
		PSNR	MS-SSIM	PSNR	PSNR
CCN [42]	TIP’20	+26.49	-21.08	+51.94	—
Cheng’20 [7]	CVPR’20	+5.58	-44.21	+7.57	+11.71
ChARM [6]	ICIP’20	+3.23	—	-0.88	—
Qian’21 [43]	ICLR’21	+10.05	-39.53	+7.52	+0.02
Xie’21 [8]	ACMMM’21	+1.55	-43.39	-0.80	+3.21
NLAIC’21 [18]	TIP’21	+11.80	-40.27	+7.11	—
Gao’21 [26]	ICCV’21	-8.76	-48.60	—	-6.49
Guo’22 [16]	TCSVT’22	-4.45	-45.23	—	—
LBHIC [17]	TCSVT’22	-4.56	-50.54	—	—
Entroformer [45]	ICLR’22	+4.73	-42.64	+2.31	-1.04
SwinT-ChARM [12]	ICLR’22	-1.73	—	—	—
NeuralSyntax [15]	CVPR’22	+8.97	-39.56	—	+5.64
STF [11]	CVPR’22	-2.48	-47.72	-2.75	+0.42
WACNN [11]	CVPR’22	-2.48	-47.72	-2.75	+0.42
ELIC [10]	CVPR’22	-5.95	-44.60	-9.14	-3.45
Contextformer [13]	ECCV’22	-5.77	-46.12	-9.05	—
GLLM [27]	TIP’23	-1.43	-47.41	-5.58	—
NVTC [60]	CVPR’23	-1.04	—	—	—
LIC-TCM Large [19]	CVPR’23	-10.14	-48.94	-11.47	-8.04
QARV [14]	TPAMI’24	+0.31	—	-3.03	—
FTIC [50]	ICLR’24	-12.99	-51.13	-14.88	-9.53
LLIC-TCM [22]	TMM’24	-10.94	-49.73	-14.99	-10.41
<b>Baseline Models</b>					
MLIC [20]	ACMMM’23	-8.05	-49.13	-12.73	-8.79
MLIC+ [20]	ACMMM’23	-11.39	-52.75	-16.38	-12.56
MLIC++ [21]	NCW ICML’23	-13.39	-53.63	-17.59	-13.08
MLICv2	Ours	<b>-16.54</b>	<b>-54.56</b>	<b>-21.61</b>	<b>-16.05</b>
MLICv2+	Ours	<b>-20.46</b>	<b>-55.86</b>	<b>-24.35</b>	<b>-19.14</b>

distribution<sup>1</sup>:

$$q_{\tau}(\mathbf{o}_{ac}^i | \Lambda_{ac}^i) \propto \begin{cases} \exp \left\{ \frac{-\operatorname{atanh}(\Lambda_{ac}^i - \lfloor \Lambda_{ac}^i \rfloor)}{\tau} \right\}, \mathbf{o}_{ac}^i = \{0, 1\}, \\ \exp \left\{ \frac{-\operatorname{atanh}(\lceil \Lambda_{ac}^i \rceil - \Lambda_{ac}^i)}{\tau} \right\}, \mathbf{o}_{ac}^i = \{1, 0\}, \end{cases} \quad (19)$$

where the temperature  $\tau = \min(0.5, e^{0.001j})$ ,  $j$  is the index of the current refine step. The temperature  $\tau$  determines how close the sample is to a true one-hot vector (lower temperatures yield samples closer to true one-hot). By decreasing  $\tau$ ,  $\Lambda_{ac}^i$  is gradually aware of the quantization, making  $(\mathbf{o}_{ac}^i)' \cdot (\lfloor \Lambda_{ac}^i \rfloor, \lceil \Lambda_{ac}^i \rceil)$  approaches discrete integers asymptotically. The refinement of  $\mathbf{y}_{na}^i$  and  $\mathbf{z}$  is the same to Equation (19). Based on SGA, the latent representation and side information are optimized by Equation (2).

## IV. EXPERIMENTS

### A. Implementation Details

1) *Training Dataset*: Our training dataset contains 101, 104 images with resolutions exceeding  $640 \times 640$  pixels. These

images are selected from various image datasets [62]–[66]. To address the existing compression artifacts in JPEG images, we follow the approach of Ballé *et al* [4] by further down-sampling the JPEG images using a randomized factor. Additionally, images with bits per pixel (bpp) lower than 3 are excluded.

2) *Training Strategy*: MLICv2 is built on Pytorch 2.2.2 [67] and CompressAI 1.2.6 [68]. Following the settings of CompressAI [68], we set  $\lambda \in \{18, 35, 67, 130, 250, 483\} \times 10^{-4}$  for MSE and set  $\lambda \in \{2.4, 4.58, 8.73, 16.64, 31.73, 60.5\}$  for Multi-Scale Structural Similarity (MS-SSIM) [69]. The models are trained on eight Tesla A100-80G GPUs with a batch size of 16. An Adam optimizer with  $\beta_1 = 0.9, \beta_2 = 0.999$  is used for training. Following Zhu *et al.* [12], the training process consists of two stages: In the first stage, we train the model with only hyperprior for 2M steps, using a learning rate of  $10^{-4}$  and a patch size of  $256 \times 256$ . This provides better initialization for the analysis and synthesis transforms. In the second stage, we load the weights of the analysis and synthesis transforms and train the full model for 2M steps. The learning rate starts at  $10^{-4}$  and decreases to  $3 \times 10^{-5}, 10^{-5}, 3 \times 10^{-6}, 10^{-6}$  at 1.5M, 1.8M, 1.9M, and 1.95M steps, respectively. We use  $256 \times 256$  patches for the first 1.2M steps, then switch to  $512 \times 512$  patches to exploit the effectiveness of global context modules. During the optimization of the guided selective compression

<sup>1</sup>[https://pytorch.org/docs/stable/\\_modules/torch/distributions/relaxed\\_categorical.html#RelaxedOneHotCategorical](https://pytorch.org/docs/stable/_modules/torch/distributions/relaxed_categorical.html#RelaxedOneHotCategorical)

TABLE II  
 ABLATION STUDIES ON KODAK. BD-RATE (%) IS EMPLOYED TO EVALUATE THEIR CONTRIBUTIONS. MLICv2<sup>+</sup> IS THE ANCHOR.

Context Modules	MLICv2 <sup>+</sup>	Case 1	Case 2	Case 3	Case 4	Case 5	Case 6	Case 7
Latent Refinement	✓	✗	✗	✗	✗	✗	✗	✗
Selective Compression	✓	✓	✗	✗	✗	✗	✗	✗
2D RoPE	✓	✓	✓	✗	✗	✗	✗	✗
Context Reweighting	✓	✓	✓	✓	✗	✗	✗	✗
Hyperprior Guided Global	✓	✓	✓	✓	✓	✗	✗	✗
Simple Token Mixing Transform	✓	✓	✓	✓	✓	✓	✗	✗
Gate	✓	✓	✓	✓	✓	✓	✓	✗
	0.00	+4.89	+5.21	+5.77	+7.79	+8.29	+9.58	+9.87



Fig. 7. Reconstructions of our proposed MLICv2, recent learned image compression models [7], [10], [11], [21] and VTM-17.0 Intra [1]. “[MSE]” denotes the model is optimized for MSE. Please zoom in for better view.

module, the selective compression module is optimized for 20K steps with a batch size of 16 and a learning rate of  $10^{-3}$ .

To enhance the instance adaptability, the latent representation and side information are further refined for 3000 steps with a learning rate of  $10^{-3}$  in MLICv2<sup>+</sup>.

### B. Benchmarks and Metrics

Following existing learned image compression models [8], [19], [21], [22], [50], we evaluate the rate-distortion performance on Kodak [35], Tecnick [36], and CLIC Pro Valid [28].

- Kodak [35] contains 24 uncompressed images with a resolution of  $768 \times 512$  pixels. It is widely used in many classic and recent learned image compression models [2], [4]–[7], [10], [20].
- Tecnick [36] is first adopted by Ballé *et al.* [4] and subsequently adopted by many follow-up works [6], [8], [13], [14], [19]–[22]. Tecnick contains 100 uncompressed images with a resolution of  $1200 \times 1200$  pixels.
- CLIC Professional Validation set (CLIC Pro Valid) [28] is the validation set utilized in the 3rd Challenge on Learned Image Compression. It consists of 41 high-resolution images, each approximately  $2048 \times 1440$  pixels. CLIC Pro Val has been extensively employed in recent methods [7], [8], [10], [11], [19], [20].

To rank the performance of learned image compression models, we employ the Bjøntegaard delta rate (BD-Rate) [70].

### C. Rate-Distortion Performance

1) *Quantitative Results*: For a fair comparison with learned image compression models, VTM-17.0 Intra is evaluated

in YUV444 color space under *encoder\_intra\_vtm.cfg*. To demonstrate the superiority of our MLICv2 and MLICv2<sup>+</sup>, we compare with recent learned image compression models [6]–[8], [10]–[13], [16]–[19], [22], [27], [42], [43], [45], [50], [60].

The rate-distortion curves are presented in Fig. 6. When compared with our baseline MLIC<sup>++</sup>, MLICv2<sup>+</sup> performs significantly better, especially at high bit-rates and on high-resolution images [28], [36]. Specifically, our MLICv2 achieves a maximum improvement of 0.6, 0.5, 0.5 dB when the bpp is around 0.8, 0.55, 0.6 on Kodak, Tecnick, CLIC Pro Val, respectively. Our MLICv2<sup>+</sup> achieves larger improvement compared to MLIC<sup>++</sup> [21] due to adopted latent refinement [34] for enhanced instance adaptability. The average improvements of latent refinement on MLICv2 on Kodak [35], Tecnick [36], CLIC Pro Val [28] are 0.22, 0.15, 0.15 dB, respectively.

BD-rate reductions over VTM-17.0 Intra are presented in Table I. Compared with existing methods, our MLICv2 and MLICv2<sup>+</sup> achieve state-of-the-art performance, reducing bd-rates by 16.54% and 20.46% on Kodak. When compared to the baseline model MLIC<sup>++</sup> [21], our MLICv2 and MLICv2<sup>+</sup> reduce 3.15% and 7.07% more bit-rates over VTM-17.0 Intra on Kodak [35], respectively. Our MLICv2 and MLICv2<sup>+</sup> also achieve superior performances on high-resolution datasets Tecnick [36] and CLIC Pro Val [28]. Specifically, our MLICv2 and MLICv2<sup>+</sup> reduce bd-rates by 21.61% and 24.35% on Tecnick [36] and 16.05% and 19.14% on CLIC Pro Val [28].

2) *Qualitative Results*: We also compare the qualitative performance to MLIC<sup>++</sup>, ELIC [10], STF, WACNN [11], Cheng’20 [7] and VTM-17.0 Intra on subjective qualities. The windowsill of reconstructions are cropped to patches for clearer

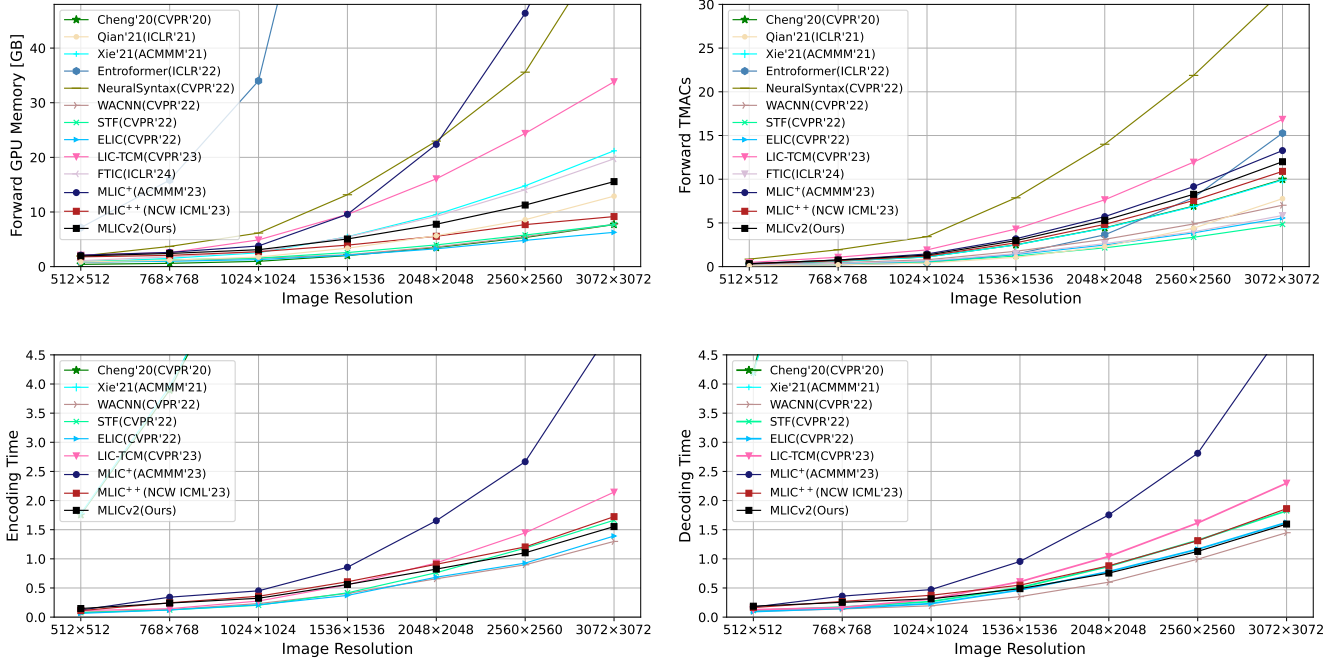


Fig. 8. GPU memory consumption, encoding time, decoding time comparisons among our proposed models [7], [8], [10], [11], [19], [45] and recent learned image compression models. Encoding and decoding time of Qian'21 [43], Entroformer [45], NeuralSyntax [15] exceed 4.5s. The encoding time and decoding time of FTIC [50] exceeds 300s due to the serial coding. The encoding time of MLICv2<sup>+</sup> exceeds 1000s due to iterative latent refinement. The decoding complexity of MLICv2<sup>+</sup> is almost the same as that of MLICv2.

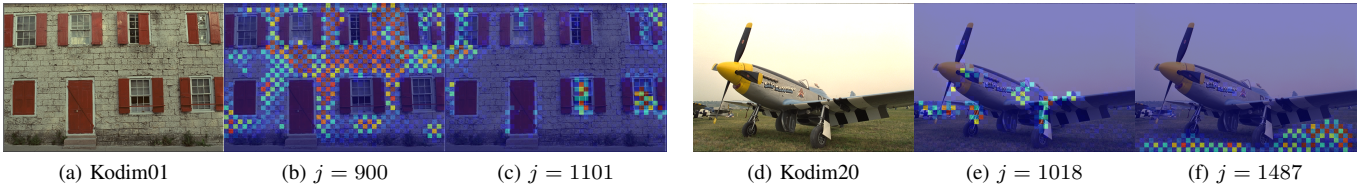


Fig. 9. Visualization of attention maps of hyperprior guided intra slice global context module. The inputs are Kodim01 and Kodim20. The attention map is computed by  $\text{Softmax}_2(\hat{\mathbf{H}}_{na,q}[j])\text{Softmax}_1(\hat{\mathbf{H}}_{ac,k})^T$ , where  $j$  is the query index.

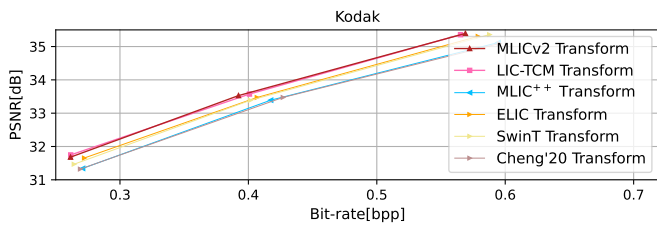


Fig. 10. Comparisons among different transforms of proposed MLICv2, LIC-TCM [19], MLIC<sup>++</sup>, ELIC [10], and Cheng'20 [7].

comparisons. The reconstructions of MLICv2 have sharper textures and retain more details. In terms of visual quality, our MLICv2 has significant improvements on rate-perception performance compared to other models.

#### D. Computational Complexity

To comprehensively evaluate model complexity, 16 images from LIU4K dataset [71] are cropped to  $\{512 \times$

$512, 768 \times 768, 1024 \times 1024, 1536 \times 1536, 2048 \times 2048, 2560 \times 2560, 3072 \times 3072\}$  patches to cover the various resolutions of images that can be encountered in reality. Forward GPU memory, encoding time, decoding time, and forward Multiply-Accumulate operations (MACs) are employed as the complexity metrics. Encoding and decoding times include arithmetic encoding and decoding times. The first three metrics are prioritized due to their direct relevance to real-world scenarios. Notably, a model with lower MACs may exhibit *slower* encoding and decoding speeds if its context module is *serial*, or consume more GPU memory. Thus, while MACs is an important complexity measure, it should be considered in conjunction with other metrics to provide a holistic understanding of the model's characteristics. Since the number of skipped elements at different bit-rates are different, we report the results of MLICv2 with  $\lambda = 0.0130$ . The model complexities are presented in Fig. 8. Please note that the complexity MLICv2<sup>+</sup> is not depicted in the Fig. 8 due to iterative latent refinement. *The decoding complexity of MLICv2<sup>+</sup> is almost the same as that of MLICv2.*

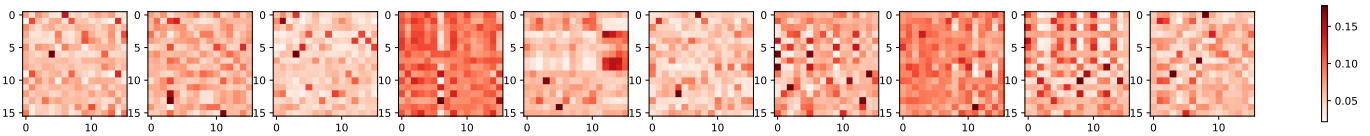


Fig. 11. Visualization of the channel weighting attention map of each attention head of  $\hat{C}_g^{<5}$  of Kodim01. Please zoom in for better view.

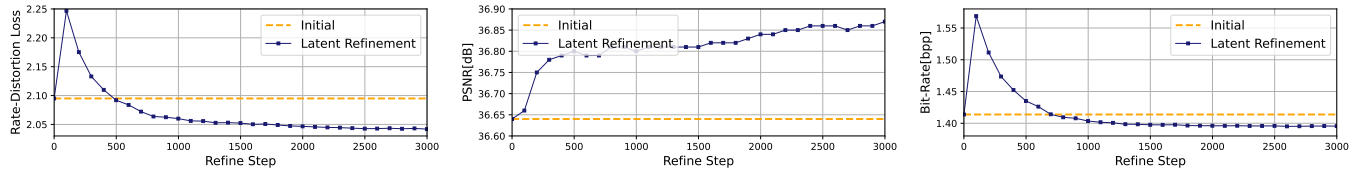


Fig. 12. Changes in loss, PSNR and bpp during the refinement of latent representation and side information of Kodim01 from Kodak dataset [35]. “Initial” denotes the original loss, psnr, bpp when using the latent representation and side information outputted by MLICv2.

1) *On Forward GPU Memory:* Compared to MLIC<sup>+</sup> [20], our MLICv2 requires significantly less memory due to its linear complexity entropy model. Compared to MLIC<sup>++</sup> [21], our MLICv2 requires slightly more memory for high-resolution images, attributable to the additional modules introduced in this paper. However, the memory assumptions of MLICv2 are still lower than those of Xie’21 [8], Qian’21 [43], Entroformer [43] and LIC-TCM [19]. This slight increase in memory usage is deemed acceptable given the performance improvements.

2) *On Forward MACs:* Compared to MLIC<sup>+</sup>, LIC-TCM [19], our MLICv2 has lower forward MACs. Compared to MLIC<sup>++</sup>, our MLICv2 exhibits slightly higher forward MACs. This increase can be attributed to two primary factors: the proposed channel reweighting module and selective compression module. However, considering the significant performance gains achieved through these enhancements, the marginal increase in MACs is deemed acceptable. The trade-off between computational complexity and improved compression efficiency is well-balanced in our proposed model.

3) *On Encoding Time and Decoding Time:* In comparison to MLIC [20], our MLICv2 demonstrates enhanced encoding and decoding efficiency, primarily attributed to its components with linear computational complexity. Furthermore, when juxtaposed with MLIC [21], MLICv2 exhibits superior performance in terms of encoding and decoding time. This improvement is largely due to MLICv2’s ability to efficiently skip most zero elements, thereby significantly reducing the time required for serial arithmetic coding. This advantage is particularly pronounced when processing high-resolution images, where the prevalence of zero elements is typically higher.

### E. Ablation Studies

1) *Settings:* In ablation studies, each model is optimized for MSE and trained using the training strategy in Section IV-A2. MLICv2<sup>+</sup> is employed as the anchor. The contribution of each module is evaluated on Kodak [35] and presented in Table II. Overall, simple token mixing transform and context reweighting are the modules with the biggest performance gains besides latent refinement.

TABLE III  
SKIP RATIO, ENCODING ACCELERATION AND DECODING ACCELERATION OF DIFFERENT QUALITY ON KODAK.

$\lambda$	0.0018	0.0035	0.0067	0.0130	0.0250	0.0483
Skip Ratio (%)	88.32	82.73	77.09	69.76	66.44	57.26
Enc Acceleration (%)	9.98	9.48	9.24	8.81	7.31	7.22
Dec Acceleration (%)	13.61	13.21	12.15	11.97	10.18	9.62

TABLE IV  
SKIP RATIO, ENCODING ACCELERATION AND DECODING ACCELERATION OF DIFFERENT QUALITY ON CLIC PRO VAL.

$\lambda$	0.0018	0.0035	0.0067	0.0130	0.0250	0.0483
Skip Ratio (%)	92.95	88.20	83.72	79.72	77.28	68.81
Enc Acceleration (%)	18.48	17.12	16.88	16.62	16.15	14.21
Dec Acceleration (%)	27.52	25.85	25.37	24.21	23.36	20.99

2) *Analysis of Enhanced Transform:* To demonstrate the effectiveness of the proposed simple token mixing block, we compare the transform module with the transform modules of Cheng’20 [7], SwinT-Charm [12], ELIC [10], and LIC-TCM [19]. The entropy model is aligned with spatial autoregressive entropy model [5]. The results are presented in Fig. 10. Our proposed transform achieves the comparable performance with LIC-TCM while with about half forward MACs. When equipped with proposed transform, the model performance gets further enhanced. Since our baseline performance is very strong, the boost from the transform is slightly small relative to Fig. 10.

3) *Analysis of Enhanced Entropy Modeling:* The guided selective compression mechanism effectively skips numerous zero elements, resulting in a reduction in bit-rate, as presented in Table II. To demonstrate the effectiveness of proposed guided selective compression on acceleration, the skip ratio, encoding acceleration and decoding acceleration on Kodak [35] and CLIC Pro Val [28] are presented in Table III and Table IV. As image quality increases, there is a concomitant decrease in the percentage of zero elements that can be skipped,

which subsequently leads to a reduction in both encoding and decoding acceleration. It is noteworthy that high-resolution images, which typically exhibit greater redundancy, allow for a higher number of elements to be skipped, thus potentially yielding more substantial acceleration benefits.

To demonstrate the effectiveness of hyperprior-guided global context for the first slice, the attention maps are illustrated in Fig. 9, which are generally accurate, thereby enhancing the performance. For slices  $\hat{y}^{\geq 1}$ , the previous one slice is still employed to predict the global correlations due to the higher bit-rate of each slice compared to the side information.

The channel reweighting maps are illustrated in Fig. 11. The varying attention scores for each channel imply differing levels of importance, allowing the entropy modeling to focus on more crucial contexts, thus improving performance.

To validate the effectiveness of the proposed 2D RoPE, the 2D RoPE is replaced by original additive relative position embedding [49]. The performance degradation caused by the replacement demonstrates the superiority of the proposed 2D RoPE.

To validate the effectiveness of the gate block, the gate block is replaced by Multilayer Perceptron (MLP), which leads to performance loss.

4) *Analysis of Enhanced Instance Adaptability*: In case 1, the latent refinement is removed, which leads to around 4.89% bit-rate increase compared to MLICv2<sup>+</sup>. The increased bit-rate demonstrates the effectiveness of the latent refinement for enhanced instance adaptability. The changes of loss, PSNR and bpp are illustrated in Fig. 12. During the refinement, the loss and bpp generally first rise and then fall to lower than the initial loss and bpp, while the PSNR generally keeps rising.

## V. CONCLUSION

In this paper, we present MLICv2 and MLICv2<sup>+</sup>, which are enhanced versions of the previous MLIC series. The motivations behind MLICv2/MLICv2<sup>+</sup> arise from observed limitations of previous MLIC series, particularly in transform, entropy modeling, and instance adaptability. To address these limitations, we propose to boost the transform by employing simple token mixing blocks while maintaining computational efficiency. For improved entropy modeling, hyperprior-based global context prediction, context reweighting and 2D rotary position embedding are employed for richer and more accurate contexts. In addition, guided selective compression is also investigated. For improved instance adaptability, stochastic Gumbel annealing [34] is employed to refine the latent iteratively. These techniques collectively result in significant performance enhancements. Furthermore, to continue improving instance adaptability, we plan to investigate the transmission of update parameters [72]–[74] to the decoder.

**Limitations**: Although our MLICv2 and MLICv2<sup>+</sup> achieve state-of-the-art performances, there are some limitations in our MLICv2 and MLICv2<sup>+</sup> to be addressed in the future work. First, MLICv2/MLICv2<sup>+</sup> may encounter cross-platform decoding issues [75]–[77], where encoded bit streams on one device may not be correctly decoded on another due to differences in floating-point computation for probabilities.

Additionally, the complexities of MLICv2/MLICv2<sup>+</sup> are still not optimal for deployment. To address these issues, we will explore model quantization techniques [78] in future work.

## REFERENCES

- [1] B. Bross, Y.-K. Wang, Y. Ye, S. Liu, J. Chen, G. J. Sullivan, and J.-R. Ohm, "Overview of the versatile video coding (vvc) standard and its applications," *IEEE TCSVT*, vol. 31, no. 10, pp. 3736–3764, 2021.
- [2] J. Ballé, V. Laparra, and E. P. Simoncelli, "End-to-end optimized image compression," in *ICLR*, 2017.
- [3] L. Theis, W. Shi, A. Cunningham, and F. Huszár, "Lossy image compression with compressive autoencoders," in *ICLR*, 2017.
- [4] J. Ballé, D. Minnen, S. Singh, S. J. Hwang, and N. Johnston, "Variational image compression with a scale hyperprior," in *ICLR*, 2018.
- [5] D. Minnen, J. Ballé, and G. D. Toderici, "Joint autoregressive and hierarchical priors for learned image compression," in *NeurIPS*, 2018, pp. 10 771–10 780.
- [6] D. Minnen and S. Singh, "Channel-wise autoregressive entropy models for learned image compression," in *ICIP*. IEEE, 2020, pp. 3339–3343.
- [7] Z. Cheng, H. Sun, M. Takeuchi, and J. Katto, "Learned image compression with discretized gaussian mixture likelihoods and attention modules," in *CVPR*, June 2020.
- [8] Y. Xie, K. L. Cheng, and Q. Chen, "Enhanced invertible encoding for learned image compression," in *ACM MM*, 2021, pp. 162–170.
- [9] D. He, Y. Zheng, B. Sun, Y. Wang, and H. Qin, "Checkerboard context model for efficient learned image compression," in *CVPR*, 2021, pp. 14 771–14 780.
- [10] D. He, Z. Yang, W. Peng, R. Ma, H. Qin, and Y. Wang, "Elic: Efficient learned image compression with unevenly grouped space-channel contextual adaptive coding," in *CVPR*, June 2022.
- [11] R. Zou, C. Song, and Z. Zhang, "The devil is in the details: Window-based attention for image compression," in *CVPR*, 2022.
- [12] Y. Zhu, Y. Yang, and T. Cohen, "Transformer-based transform coding," in *ICLR*, 2022.
- [13] A. B. Koyuncu, H. Gao, A. Boev, G. Gaikov, E. Alshina, and E. Steinbach, "Contextformer: A transformer with spatio-channel attention for context modeling in learned image compression," in *ECCV*, 2022, pp. 447–463.
- [14] Z. Duan, M. Lu, J. Ma, Y. Huang, Z. Ma, and F. Zhu, "Qarv: Quantization-aware resnet vae for lossy image compression," *IEEE TPAMI*, vol. 46, no. 1, pp. 436–450, 2024.
- [15] D. Wang, W. Yang, Y. Hu, and J. Liu, "Neural data-dependent transform for learned image compression," in *CVPR*, 2022.
- [16] Z. Guo, Z. Zhang, R. Feng, and Z. Chen, "Causal contextual prediction for learned image compression," *IEEE TCSVT*, vol. 32, no. 4, pp. 2329–2341, 2022.
- [17] Y. Wu, X. Li, Z. Zhang, X. Jin, and Z. Chen, "Learned block-based hybrid image compression," *IEEE TCSVT*, vol. 32, no. 6, pp. 3978–3990, 2022.
- [18] T. Chen, H. Liu, Z. Ma, Q. Shen, X. Cao, and Y. Wang, "End-to-end learnt image compression via non-local attention optimization and improved context modeling," *IEEE TIP*, vol. 30, pp. 3179–3191, 2021.
- [19] J. Liu, H. Sun, and J. Katto, "Learned image compression with mixed transformer-cnn architectures," in *CVPR*, 2023.
- [20] W. Jiang, J. Yang, Y. Zhai, P. Ning, F. Gao, and R. Wang, "Mlic: Multi-reference entropy model for learned image compression," in *ACM MM*, 2023.
- [21] W. Jiang and R. Wang, "Mlic++: Linear complexity multi-reference entropy modeling for learned image compression," in *ICML 2023 Workshop Neural Compression: From Information Theory to Applications*, 2023. [Online]. Available: <https://openreview.net/forum?id=hxIpcSoz2t>
- [22] W. Jiang, P. Ning, J. Yang, Y. Zhai, F. Gao, and R. Wang, "Llic: Large receptive field transform coding with adaptive weights for learned image compression," *IEEE TMM*, pp. 1–15, 2024.
- [23] W. Duan, Z. Chang, C. Jia, S. Wang, S. Ma, L. Song, and W. Gao, "Learned image compression using cross-component attention mechanism," *IEEE TIP*, 2023.
- [24] J. Guo, D. Xu, and G. Lu, "Cbanet: Toward complexity and bitrate adaptive deep image compression using a single network," *IEEE TIP*, vol. 32, pp. 2049–2062, 2023.
- [25] G. E. Hinton and R. Zemel, "Autoencoders, minimum description length and helmholtz free energy," *NeurIPS*, vol. 6, 1993.
- [26] G. Gao, P. You, R. Pan, S. Han, Y. Zhang, Y. Dai, and H. Lee, "Neural image compression via attentional multi-scale back projection and frequency decomposition," in *ICCV*, 2021, pp. 14 677–14 686.

- [27] H. Fu, F. Liang, J. Lin, B. Li, M. Akbari, J. Liang, G. Zhang, D. Liu, C. Tu, and J. Han, "Learned image compression with gaussian-laplacian-logistic mixture model and concatenated residual modules," *IEEE TIP*, vol. 32, pp. 2063–2076, 2023.
- [28] G. Toderici, W. Shi, R. Timofte, L. Theis, J. Ballé, E. Agustsson, N. Johnston, and F. Mentzer, "Workshop and challenge on learned image compression (elic2020)," *CVPR*, 2020.
- [29] T. Xu, Y. Wang, D. He, C. Gao, H. Gao, K. Liu, and H. Qin, "Multi-sample training for neural image compression," *NeurIPS*, vol. 35, pp. 1502–1515, 2022.
- [30] G. J. Sullivan and T. Wiegand, "Rate-distortion optimization for video compression," *IEEE SPM*, vol. 15, no. 6, pp. 74–90, 1998.
- [31] E.-H. Yang and X. Yu, "Rate distortion optimization for h. 264 interframe coding: A general framework and algorithms," *IEEE TIP*, vol. 16, no. 7, pp. 1774–1784, 2007.
- [32] I. Choi, J. Lee, and B. Jeon, "Fast coding mode selection with rate-distortion optimization for mpeg-4 part-10 avc/h. 264," *IEEE TCSVT*, vol. 16, no. 12, pp. 1557–1561, 2006.
- [33] W. Yu, M. Luo, P. Zhou, C. Si, Y. Zhou, X. Wang, J. Feng, and S. Yan, "Metaformer is actually what you need for vision," in *CVPR*, 2022, pp. 10 819–10 829.
- [34] Y. Yang, R. Bamler, and S. Mandt, "Improving inference for neural image compression," *NeurIPS*, vol. 33, pp. 573–584, 2020.
- [35] E. Kodak, "Kodak lossless true color image suite," 1993.
- [36] N. Asuni and A. Giachetti, "Testimages: a large-scale archive for testing visual devices and basic image processing algorithms," in *STAG*, 2014.
- [37] J. Ballé, V. Laparra, and E. P. Simoncelli, "Density modeling of images using a generalized normalization transformation," *ICLR*, 2015.
- [38] Y. Zhang, K. Li, K. Li, B. Zhong, and Y. Fu, "Residual non-local attention networks for image restoration," in *ICLR*, 2019.
- [39] M. Lu, P. Guo, H. Shi, C. Cao, and Z. Ma, "Transformer-based image compression," in *DCC*, 2022, pp. 469–469.
- [40] Z. Cui, J. Wang, S. Gao, T. Guo, Y. Feng, and B. Bai, "Asymmetric gained deep image compression with continuous rate adaptation," in *CVPR*, June 2021, pp. 10 532–10 541.
- [41] A. Van den Oord, N. Kalchbrenner, L. Espeholt, O. Vinyals, A. Graves *et al.*, "Conditional image generation with pixelcnn decoders," *NeurIPS*, vol. 29, 2016.
- [42] M. Li, K. Ma, J. You, D. Zhang, and W. Zuo, "Efficient and effective context-based convolutional entropy modeling for image compression," *IEEE TIP*, vol. 29, pp. 5900–5911, 2020.
- [43] Y. Qian, Z. Tan, X. Sun, M. Lin, D. Li, Z. Sun, L. Hao, and R. Jin, "Learning accurate entropy model with global reference for image compression," in *ICLR*, 2020.
- [44] J.-H. Kim, B. Heo, and J.-S. Lee, "Joint global and local hierarchical priors for learned image compression," in *CVPR*, 2022.
- [45] Y. Qian, M. Lin, X. Sun, Z. Tan, and R. Jin, "Entroformer: A transformer-based entropy model for learned image compression," in *ICLR*, 2022.
- [46] W. Jiang, J. Li, K. Zhang, and L. Zhang, "Lvc-igmc: Joint local and global motion compensation for learned video compression," in *ICASSP*. IEEE, 2024, pp. 2955–2959.
- [47] Z. Shen, M. Zhang, H. Zhao, S. Yi, and H. Li, "Efficient attention: Attention with linear complexities," in *WACV*, 2021.
- [48] W. Jiang, J. Li, K. Zhang, and L. Zhang, "Ecv: Exploiting non-local correlations in multiple frames for contextual video compression," in *CVPR*, 2025.
- [49] Z. Liu, Y. Lin, Y. Cao, H. Hu, Y. Wei, Z. Zhang, S. Lin, and B. Guo, "Swin transformer: Hierarchical vision transformer using shifted windows," in *ICCV*, October 2021, pp. 10 012–10 022.
- [50] H. Li, S. Li, W. Dai, C. Li, J. Zou, and H. Xiong, "Frequency-aware transformer for learned image compression," in *ICLR*, 2024, pp. 1–11.
- [51] J. L. Ba, J. R. Kiros, and G. E. Hinton, "Layer normalization," *arXiv preprint arXiv:1607.06450*, 2016.
- [52] J. Su, M. Ahmed, Y. Lu, S. Pan, W. Bo, and Y. Liu, "Roformer: Enhanced transformer with rotary position embedding," *Neurocomputing*, vol. 568, p. 127063, 2024.
- [53] H. Touvron, T. Lavril, G. Izacard, X. Martinet, M.-A. Lachaux, T. Lacroix, B. Rozière, N. Goyal, E. Hambro, F. Azhar *et al.*, "Llama: Open and efficient foundation language models," *arXiv preprint arXiv:2302.13971*, 2023.
- [54] M. Reid, N. Savinov, D. Teplyashin, D. Lepikhin, T. Lillicrap, J.-b. Alayrac, R. Soricut, A. Lazaridou, O. Firat, J. Schrittwieser *et al.*, "Gemini 1.5: Unlocking multimodal understanding across millions of tokens of context," *arXiv preprint arXiv:2403.05530*, 2024.
- [55] A. Vaswani, N. Shazeer, N. Parmar, J. Uszkoreit, L. Jones, A. N. Gomez, Ł. Kaiser, and I. Polosukhin, "Attention is all you need," *NeurIPS*, vol. 30, pp. 5998–6008, 2017.
- [56] A. Ali, H. Touvron, M. Caron, P. Bojanowski, M. Douze, A. Joulin, I. Laptev, N. Neverova, G. Synnaeve, J. Verbeek *et al.*, "Xcit: Cross-covariance image transformers," *NeurIPS*, vol. 34, pp. 20 014–20 027, 2021.
- [57] J. Lee, S. Jeong, and M. Kim, "Selective compression learning of latent representations for variable-rate image compression," *NeurIPS*, vol. 35, pp. 13 146–13 157, 2022.
- [58] D. Alexandre, H.-M. Hang, and W.-H. Peng, "Hierarchical b-frame video coding using two-layer canf without motion coding," in *CVPR*, 2023, pp. 10 249–10 258.
- [59] Y. Shi, Y. Ge, J. Wang, and J. Mao, "Alphavc: High-performance and efficient learned video compression," in *ECCV*, 2022, pp. 616–631.
- [60] R. Feng, Z. Guo, W. Li, and Z. Chen, "Nvtc: Nonlinear vector transform coding," in *CVPR*, June 2023, pp. 6101–6110.
- [61] D. P. Kingma and J. Ba, "Adam: A method for stochastic optimization," in *ICLR*, 2015.
- [62] J. Deng, W. Dong, R. Socher, L.-J. Li, K. Li, and L. Fei-Fei, "Imagenet: A large-scale hierarchical image database," in *CVPR*. IEEE, 2009, pp. 248–255.
- [63] T.-Y. Lin, M. Maire, S. Belongie, J. Hays, P. Perona, D. Ramanan, P. Dollár, and C. L. Zitnick, "Microsoft coco: Common objects in context," in *ECCV*, 2014, pp. 740–755.
- [64] E. Agustsson and R. Timofte, "Ntire 2017 challenge on single image super-resolution: Dataset and study," *CVPR Workshops*, pp. 1122–1131, 2017.
- [65] B. Lim, S. Son, H. Kim, S. Nah, and K. Mu Lee, "Enhanced deep residual networks for single image super-resolution," in *CVPR Workshops*, 2017, pp. 136–144.
- [66] Q. Yang, D. Chen, Z. Tan, Q. Liu, Q. Chu, J. Bao, L. Yuan, G. Hua, and N. Yu, "Hq-50k: A large-scale, high-quality dataset for image restoration," *arXiv preprint arXiv:2306.05390*, 2023.
- [67] A. Paszke, S. Gross, F. Massa, A. Lerer, J. Bradbury, G. Chanan, T. Killeen, Z. Lin, N. Gimelshein, L. Antiga *et al.*, "Pytorch: An imperative style, high-performance deep learning library," in *NeurIPS*, 2019, pp. 8024–8035.
- [68] J. Bégin, F. Racapé, S. Feltman, and A. Pushparaja, "Compressai: a pytorch library and evaluation platform for end-to-end compression research," *arXiv preprint arXiv:2011.03029*, 2020.
- [69] Z. Wang, E. P. Simoncelli, and A. C. Bovik, "Multiscale structural similarity for image quality assessment," in *ACSSC*, vol. 2. IEEE, 2003.
- [70] G. Bjontegaard, "Calculation of average psnr differences between rd-curves," *ITU SG16 Doc. VCEG-M33*, 2001.
- [71] J. Liu, D. Liu, W. Yang, S. Xia, X. Zhang, and Y. Dai, "A comprehensive benchmark for single image compression artifact reduction," *IEEE TIP*, vol. 29, pp. 7845–7860, 2020.
- [72] K. Tsubota, H. Akutsu, and K. Aizawa, "Universal deep image compression via content-adaptive optimization with adapters," in *WACV*, 2023, pp. 2529–2538.
- [73] S. Shen, H. Yue, and J. Yang, "Dec-adapter: Exploring efficient decoder-side adapter for bridging screen content and natural image compression," in *ICCV*, 2023, pp. 12 887–12 896.
- [74] Y. Lv, J. Xiang, J. Zhang, W. Yang, X. Han, and W. Yang, "Dynamic low-rank instance adaptation for universal neural image compression," in *ACM MM*, 2023, pp. 632–642.
- [75] J. Ballé, N. Johnston, and D. Minnen, "Integer networks for data compression with latent-variable models," in *ICLR*, 2019.
- [76] D. He, Z. Yang, Y. Chen, Q. Zhang, H. Qin, and Y. Wang, "Post-training quantization for cross-platform learned image compression," *arXiv preprint arXiv:2202.07513*, 2022.
- [77] J. Shi, M. Lu, and Z. Ma, "Rate-distortion optimized post-training quantization for learned image compression," *IEEE TCSVT*, 2023.
- [78] S. Han, H. Mao, and W. J. Dally, "Deep compression: Compressing deep neural networks with pruning, trained quantization and huffman coding," in *ICLR*, 2016.